ORIGINAL RESEARCH ARTICLE

Phase Stability and Deformation Modes in Functionally Graded Metastable Austenitic Stainless Steel; A Novel Approach to Evaluate the Role of Nitrogen

BO WANG, KONSTANTIN V. WERNER, MATTEO VILLA, THOMAS L. CHRISTIANSEN, and MARCEL A.J. SOMERS

An austenitic stainless steel AISI 304 plate was functionally graded by interstitial alloying with nitrogen by high-temperature solution nitriding, resulting in a symmetrical nitrogen concentration profile over the plate thickness. The responses to plastic deformation and austenite stability were investigated by applying cold rolling up to 70 pct overall thickness reduction of the plate. Electron probe microanalysis, X-ray diffraction, electron microscopy, and hardness indentation were applied for characterization of the evolutions of nitrogen concentration profile, phase distribution, deformation microstructure, and hardness developing upon plastic deformation. The results demonstrate that the critical nitrogen content necessary to prevent deformation-induced martensite formation increases in the low-to-medium strain range, while it dramatically increases at high strain levels. With increasing nitrogen content, the dominant deformation mode evolves from deformation-induced martensite formation to a mixture of martensite and twin formation, and, eventually twinning and dislocation glide. The plastic strain regimes for the various deformation modes depend strongly on the nitrogen content. The results are discussed in relation to the effect of nitrogen content on the stacking fault energy of austenite in Fe–Cr–Ni alloys.

https://doi.org/10.1007/s11661-022-06904-x

I. INTRODUCTION

CONVENTIONAL metastable austenitic stainless steels (MAUSS), such as AISI 304, find wide industrial application due to their superior toughness and extraordinary formability.[1] The inherent metastable nature of MAUSS implies that plastic straining can cause deformation-induced martensite formation, the so-called transformation-induced plasticity (TRIP) effect.[2–5] Such deformation-induced martensite suffers from relatively low ductility, and leads to poor corrosion performance in certain cases.[6–8] Generally, in industrial practice, a series of metal forming processing steps is succeeded by solution annealing as the final treatment to restore the stainless and non-magnetic properties that were compromised by the deformation. Relatively low strength in the solution-annealed state is a potential drawback for many industrial applications.

Another phenomenon that can occur during plastic straining of metals is the twinning-induced plasticity (TWIP) effect. In the case of Fe–Cr–Ni MAUSS, TWIP can be promoted by alloying with austenite stabilizers such as nickel,[9,10] carbon,[11] and nitrogen.[6,7,12,13] Despite a somewhat lower tensile strength than in the case of TRIP, TWIP brings about higher ductility, and particularly, leads to significant improvement in the resistance against aqueous corrosion, because no martensite develops. In addition, combining TWIP and TRIP effects, which typically occurs in austenitic (non-stainless) manganese steels, offers attractive mechanical properties, combining high strength and high ductility.[14] In principle, this combination can also be achieved in MAUSS by tailoring the composition.

For Fe–Cr–Ni MAUSS, nitrogen has a higher solubility than carbon and offers an effective solid-solution strengthening effect, combined with improved localized corrosion resistance (pitting and crevice corrosion).[13,15,16] Furthermore, nitrogen in solid-solution is a more effective and cheap austenite stabilizer than expensive nickel.[16] Therefore, in the past decades,

BO WANG, KONSTANTIN V. WERNER, MATTEO VILLA, THOMAS L. CHRISTIANSEN and MARCEL A. J. SOMERS are with the Department of Mechanical Engineering, Technical University of Denmark, Kongens Lyngby 2800, Denmark. Contact: e-mail: bwang@mek.dtu.dk
Manuscript submitted June 9, 2022; accepted November 6, 2022.
Article published online December 11, 2022

nitrogen-alloyed MAUSS (*e.g.*, 304N/1.4315) or high nitrogen austenitic stainless steels (> 0.40 wt pct N) have received attention as a promising class of engineering materials.[17] Due to the improved mechanical properties and, especially, better resistance to intergranular and localized corrosion, nitrogen-alloyed MAUSS have been regarded as an appropriate substitute for 300 series stainless steels in certain engineering applications.[15] Essentially, the service properties of such materials are associated with improved stabilization of austenite, improved strength, and improved corrosion resistance. For a certain nitrogen content, austenite stability against deformation-induced martensite formation depends on the applied strain.[18,19] The dependence of phase stability on the combination of nitrogen content and plastic strain needs further investigation to arrive at clear alloy design criteria, also in connection with specific forming operations.

In MAUSS, the deformation mechanism was demonstrated to depend on the nitrogen content and changes from TRIP to TWIP to dislocation glide (slip) with increasing nitrogen content. Generally, it is considered that the deformation mechanism in austenitic steels depends on the stacking fault energy (SFE).[20,21] SFE is commonly considered an intrinsic material property and its experimental value depends on composition and grain size.[22] The current paradigm in austenitic steels is that, with increasing SFE (range), the deformation mechanism changes from TRIP (SFE < 20 $mJ{\cdot}m^{-2}$) to TWIP (~ 20 to 45 $mJ{\cdot}m^{-2}$) to slip (> 45 $mJ{\cdot}m^{-2}$).[23–25] This suggests that, for a particular straining condition, the three specific ranges of nitrogen content can be distinguished, corresponding to the abovementioned SFE regimes characteristic for the three deformation modes. Changing the strain level influences these nitrogen content ranges and, hence, modifies the critical nitrogen contents marking the TRIP/TWIP and TWIP/slip transitions. Further clarification of the variation of SFE in a continuous range of nitrogen contents appears, however, necessary at this stage, since the effect of N on the SFE is ambiguous.[9,26] This is a motivation for investigating a continuous range of nitrogen contents for a fixed substitutional composition with various plastic strains.

High-temperature solution nitriding (HTSN) was originally introduced by Berns[27,28] in the nineties of the previous century and entails controlled nitrogen dissolution into stainless steels at 1100 ± 50 °C in N_2 gas. The treatment is intended to bring about a precipitate-free nitrogen-enriched case. Also, it can be used for the synthesis of thin plate high nitrogen steel with uniform composition.[29] The process parameters of solution nitriding are temperature, partial pressure of N_2 in the gas, and treatment time. If no through-nitriding is achieved, the resulting solution-nitrided case, in which the nitrogen concentration gradually decreases with distance from the surface, establishes a continuous range of N contents in austenite. Applying plastic deformation on such a composition profile offers an extensive, albeit complex, picture for investigating nitrogen alloying and plastic straining.

In the present study, metastable austenitic stainless steel plates were solution nitrided from both sides to achieve a depth gradient in nitrogen content that is symmetric with respect to the central plane of the plate. Subsequently, the plates were cold rolled (CR). The austenite stability dependence on nitrogen content was assessed for various cold rolling reductions from quantitative estimates of the volume fraction of deformation-induced martensite. The threshold nitrogen content to avoid martensite formation for each rolling condition was determined by locating the depth beyond which martensite was detected. The deformation mechanisms were assessed from the microstructural features (martensite, twins, and dislocations) in relation to the nitrogen content and cold rolling reduction. In addition to information of fundamental interest, the work illustrates a method to functionally grade this technologically important material, so that final products can be obtained after cold rolling of nitrogen-alloyed sheets where a martensite-free (*i.e.,* non-magnetic and corrosion-resistant) and hard (wear-resistant) surface can be obtained without compromising the formability of the material.

II. EXPERIMENTAL PROCEDURE

The material used in this study is a commercial 304 stainless steel with chemical composition (in wt pct): 0.058 C, 18.09 Cr, 7.89 Ni, 1.07 Mn, 0.54 Si, 0.024 N, balanced by Fe. The 304 stainless steel was received as plates, with dimensions of 60 × 25 × 2.9 mm^3, in annealed condition. The steel plates were solution nitrided at 1150 °C (1423 K) for 2 h in 0.5 bar N_2 (total pressure) gas in a custom-built Kanthal tube furnace. The solution nitriding conditions were deliberately chosen to avoid through-nitriding of the plate. Instead, a symmetric nitrogen concentration profile was obtained by nitrogen ingress from both sides of the plate. To avoid austenite decomposition and/or the formation of nitrides after high-temperature treatment, high-pressure (N_2) gas cooling was applied. Thermo-Calc 2017b with the TCFE steels/Fe v6.2 database was used to calculate an isopleth of the steel composition showing only a change in nitrogen content and temperature. In addition, the iso-activity line for the applied gas pressure was calculated in relation to temperature. Typical examples of such isopleths with superimposed iso-activity lines can be found in References 12 and 29. The calculated equilibrium nitrogen content for the steel composition and the HTSN conditions is 0.42 wt pct N in austenite, which is the composition expected at the surface. The HTSN-treated plates were uni-directionally rolled in a two-high rolling mill under oil lubrication at room temperature. The thickness reduction in a single rolling pass was about 150 μm. Cold rolling reductions of 20 to 70 pct were achieved by multi-pass cold rolling, *i.e.*, an appropriate series of single passes.

For microstructure analysis, specimens measuring 15 × 8 mm^2 were cut from the center part of the plates; the thickness of the specimens is in the range 0.87 to 2.32 mm, depending on the applied rolling reduction.

Cross-sections used for light microscopical analysis were ground, polished, and etched with Kalling's reagent for 5 to 30 s. In general, the higher the degree of deformation, the shorter was the required etching time. The cross-sectional microstructures in as-annealed, solution nitrided, and deformed states were investigated with a Zeiss Jena Neophot 30 microscope. The microstructural evolution along the normal direction (ND) was further investigated on cross sections of the solution-nitrided and deformed specimens using a combination of electron channeling contrast imaging (ECCI) and electron backscatter diffraction (EBSD) on a Zeiss Supra 35 scanning electron microscope (SEM). The cross-sections were electropolished in "Struers Electrolyte A2" at 25 V for ~ 20 s in a Struers LectroPol-5 electrolytic polishing machine prior to ECCI/EBSD analysis. ECC images contain information on the deformation microstructure in the solution-nitrided case and were taken in the core at 15 kV accelerating voltage and ~ 5 mm working distance. EBSD analysis was performed using a step size of 50 nm, an accelerating voltage of 20 kV, and a working distance of 13 mm; the angle between incoming electron beam and surface normal to the specimen was 70°.

X-ray diffraction (XRD) for phase identification was carried out on a Bruker D8 AXS X-ray diffractometer equipped with Cr radiation. Prior to XRD investigation, no additional mechanical preparation was applied. Phase identification at the surface was performed in the scattering angle range 60 to 160 deg 2θ at a 0.03 deg 2θ step size and 4 s counting time per 2θ step. To study the structures along the ND using XRD investigation, the specimen was examined at different depths by removing 15 to 25 μm thin layers by electropolishing. The diffractograms at different depths were acquired in the range 60 to 160 deg 2θ at a 0.06 deg 2θ step size and 1 s step time. Based on the X-ray diffractograms at different depths, the in-depth distribution of the volume fraction of deformation-induced martensite was quantitatively estimated using the direct comparison method.[30,31] In the quantification procedure, the variation in diffraction peak intensity, as induced by rolling texture, was averaged according to intensities of a texture-free powder mixture measured at χ tilts ranging from 0 to 70 deg at 5 deg increments, in both rolling direction (RD) and transverse direction (TD). Pure iron powder with an average particle size of ~ 10 μm was used as texture-free reference for ferrite (α'-martensite); a 316 stainless steel powder with a mean particle size of ~ 32 μm was used as the austenite reference. The integrated peak areas under the XRD profiles of the γ-austenite (FCC) peaks 111, 200, and 220, and the α'-martensite (BCC) peaks 110, 200, and 211 were considered.

Nitrogen concentration distributions were measured along traces perpendicular to the specimen surface with a 1610 Electron Probe Microanalyzer (EPMA-1610, SHIMADZU, Japan) equipped with five wavelength-dispersive X-ray spectrometers. The incident electron beam was operated at an acceleration voltage of 15 kV, a beam current of 100 nA, and a beam size of 5 μm. Sampling time was 80 ms; a LS8E dispersive crystal (2d spacing ~ 8 nm) was used to select the N K_α X-ray line. Quantification of the nitrogen content was achieved by comparison to a calibration curve for the N K_α line peak intensity in reference steels with nitrogen contents in the range of 0 to 0.90 wt pct. Hardness–depth profiles of specimens in solution-nitrided and cold-rolled conditions were measured on a Futuretech FM700 hardness tester applying a 25 g load and a 10 s dwelling time. The hardness values presented are the average of 6 individual measurements obtained at the same depth.

III. RESULTS

A. *Solution Nitriding*

The nitrogen concentration–depth profile that has developed during HTSN of the 304 steel is shown in Figure 1(a) and demonstrates that nitrogen is effectively dissolved to a depth of about 750 μm. Fitting the solution to Fick's 2nd law for diffusion into a semi-infinite medium with constant diffusion coefficient of nitrogen in austenite, D_N^γ, it is obtained: $D_N^\gamma = (1.25 \pm 0.03)\ 10^{-11}\ m^2 \cdot s^{-1}$. The experimentally determined N concentration close to the surface is in excellent agreement with the predicted equilibrium content of 0.42 wt pct N (see Experimental).

Figure 1(b) gives the X-ray diffractograms of 304 stainless steel in annealed and solution-nitrided conditions. The tiny diffraction peak of ferrite (or α'-martensite) present in an annealed steel disappears upon solution nitriding, and a fully austenitic structure develops with no indications of the presence of chromium nitride. The occurrence of grain growth during solution nitriding is evident from the light optical images shown in Figures 1(c) and (d). Since both dissolving nitrogen and the application of a high-temperature stabilized mono-phase austenite, remnants of ferrite or martensite readily dissolve during solution nitriding. The banded microstructure in the annealed condition (Figure 1(c)), which is suspected to contain retained δ-ferrite[1] along regions with locally higher chromium contents, is largely absent in the solution-nitrided state, consistent with the disappearance of ferrite from the diffractogram (Figure 1(b)). The precipitate-free grain boundaries and grain interiors are consistent with the thermodynamics prediction that no Cr-nitrides form during solution nitriding[12] and confirm that cooling was sufficiently fast to prevent precipitation of Cr-nitrides from supersaturated solid solution. After HTSN, a non-nitrided core of austenite is sandwiched between two nitrogen-alloyed austenite cases. A functional gradient in nitrogen content from surface to core is anticipated to lead to a depth gradient of the materials' properties, as for example the yield strength.

B. *Cold Deformation of Solution-Nitrided 304 Steel Plates*

1. *Strain inhomogeneity in the solution-nitrided zone*

Cold rolling after HTSN affects the in-depth nitrogen distribution. Figure 2(a) shows the evolution of nitrogen

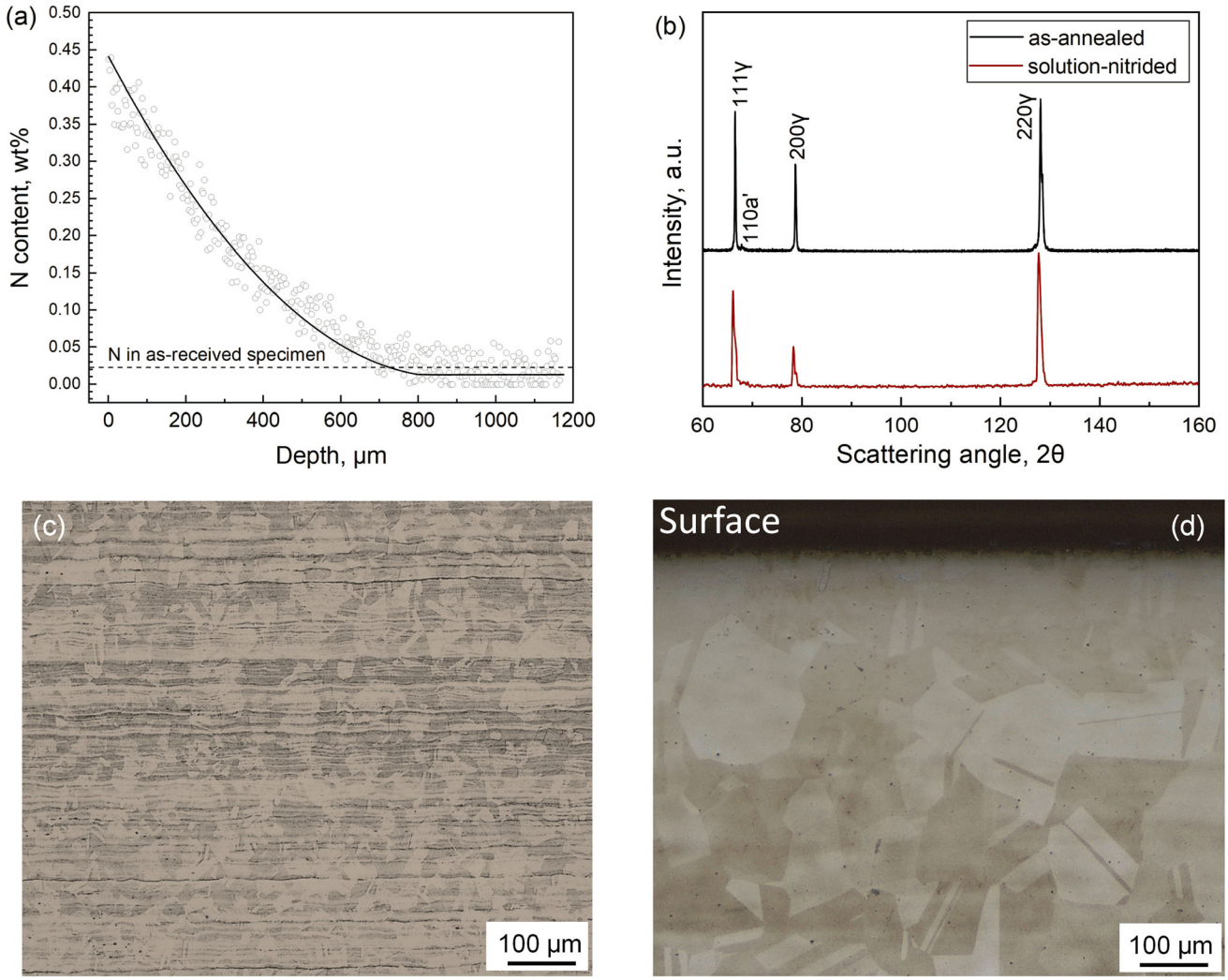

Fig. 1—(*a*) Nitrogen–depth profile in 304 stainless steel after solution nitriding. The dashed line indicates the nitrogen content in the as-delivered material. (*b*) X-ray diffractograms showing phase and texture change, both of which are associated with the dissolution of nitrogen. Light optical microstructures of 304 stainless steel in (*c*) annealed and (*d*) solution-nitrided state.

concentration–depth profiles after 20 to 70 pct cold rolling. The nitrogen distribution becomes more compressed with increasing reduction of the plate thickness. The fitted nitrogen concentration profiles provide the reduction in case depth as a function of the total reduction in plate thickness. The case/core transition was taken as the beginning of the plateau. Subtracting the case depth for both sides of the plate from the total remaining thickness of the plate yields the reduction of the core thickness. The reductions in case depth and remaining core thickness are shown as a function of the total thickness reduction of the plate in Figure 2(b). For all cold rolling conditions, the accumulated reduction (in pct) of the case depth is smaller than the total thickness reduction (in pct) of the plate, while a higher reduction (in pct) exists in the core. The strain inhomogeneity is particularly pronounced for relatively small overall strains. For thickness reductions exceeding 60 pct, additional plastic deformation is primarily accommodated by the case (Figure 2(b)). The difference in cold rolling response of the case and the core is ascribed to different mechanical properties in case and core, as resulting from the difference in N content. Changing the nitrogen content affects the austenite stability, the prevalent deformation mechanism at a given strain, the associated work hardening behavior and the local yield strength. Plasticity concentrates in certain regions as a function of the characteristics of the applied forming process in combination with the local strength of the material arising from both solid solution strengthening and work hardening.

The determined nitrogen–depth profiles after cold rolling can be used to assess the local degree of deformation. Specifically, the cold-rolling-induced shift of the depth where a particular nitrogen content occurs reflects the actual reduction at this depth, *i.e.*, plastic strain. Accordingly, the strain distribution as a function of the nitrogen content and as a function of depth are obtained, as presented in Figures 3(a) and (b), respectively. For all strain distribution curves in Figure 3(a), 0.4 wt pct was chosen as the N content close to the surface zone, while 0.024 wt pct was chosen as the last

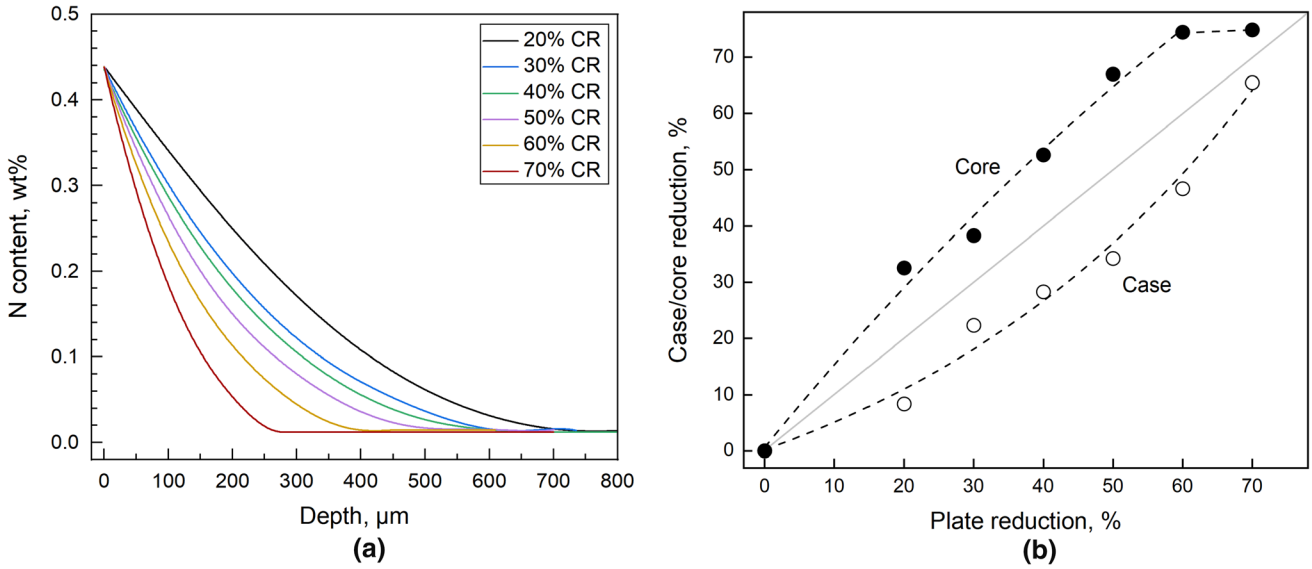

Fig. 2—(*a*) Nitrogen concentration–depth profiles of 304 steel after solution nitriding and 20 to 70 pct cold rolling. (*b*) Reductions of case depth and core thickness in relation to the overall thickness reduction of the plate.

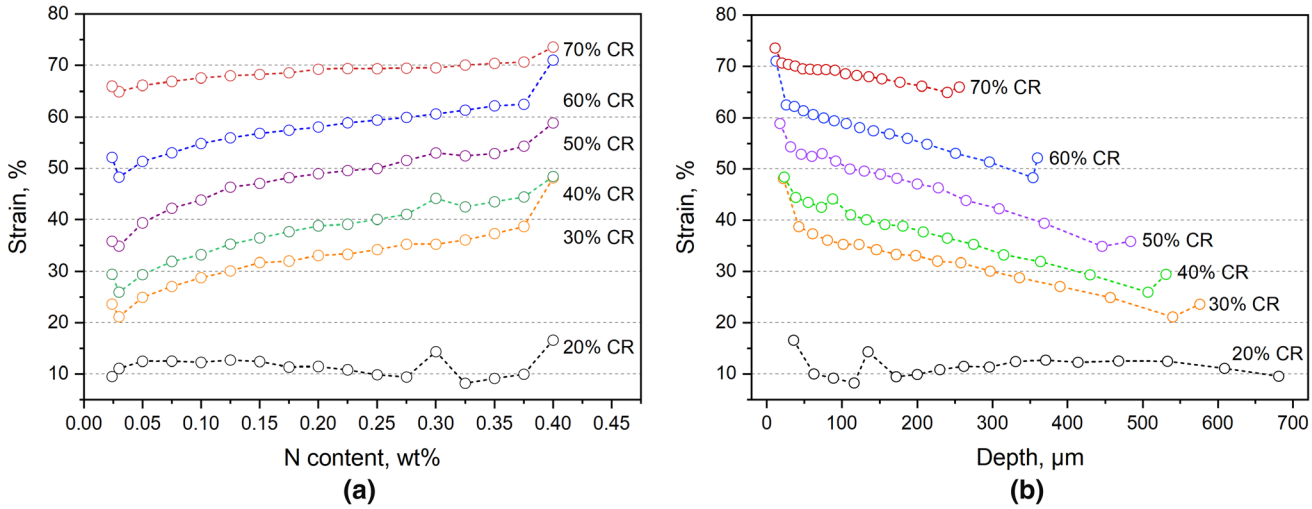

Fig. 3—Strain distribution in the solution-nitrided zone (the case) as a function of (*a*) nitrogen content and (*b*) depth for the various cold rolling reductions.

point corresponding to the N content at the case/core transition. The starting depth in Figure 3(b) for 0.4 wt pct N varies from ~ 36 to 11 μm in the applied cold rolling reduction range 20 to 70 pct. Obviously, for all rolling conditions, the strain distribution over the case depth is inhomogeneous. Generally, also for homogeneous materials, cold rolling can result in a non-uniform strain distribution over the plate thickness, depending on the applied rolling conditions, *e.g.*, friction conditions between plate and work roll, feeding speed, total reduction, *etc.*[32,33] Furthermore, texture changes in the plate upon HTSN (and subsequent deformation) and formation of strain-induced martensite bring about locally inhomogeneous and unstable strain.[34] As compared to homogeneous materials, the change in microstructure and properties along with changing N content contribute to the non-uniform deformation response over the plate thickness.

After 4 rolling passes, a total thickness reduction of 20 pct was achieved, while the actual strain in the solution-nitrided case fluctuates around 10 pct (Figure 3). This considerably smaller strain in the case is associated with the higher yield strength in the case as compared to the yield strength in the core, such that the thickness reduction is largely achieved by plastic straining in the core (see Figure 2(b)). For larger rolling reductions (30 to 70 pct), the local strain near the surface (0.4 wt pct N) is significantly higher than corresponding to the total thickness reduction, despite a mean strain in the case well below the total thickness reduction, *i.e.*, the global strain.

This phenomenon is consistent with the observation for homogeneous materials, and is ascribed to the strong shearing that typically occurs in the surface during rolling, resulting in strain maxima close to the surface. The affected zone ranges from a few to several tens of microns. As follows from Figure 3(b), the local strain gradually decreases with depth, until it reaches the case/core transition, from whereon an increase in strain with depth is observed for most of the specimens. This trend is anticipated to continue in the core, in order to obtain an average strain level in the core that exceeds the overall average reduction (see Figure 2(b)). Evidently, an increase in the thickness reduction promotes conditions in the material that are favorable for a concentration of strains (and stresses) near the surface. Consistently, it is noted that the depth (or N content) where a strain equals the total thickness reduction, shifts towards the surface (or higher N contents) with increasing rolling reduction. The observed evolution of the strain distribution with cold rolling reduction is related to the combined effects of nitrogen on the yield strength, the work hardening rate, and the operating deformation mechanisms (see below). For example, in the sub-surface zone, more strain-induced martensite will form along with more accumulated thickness reduction. The considerably higher accumulated strain in the core in an early stage of cold rolling (≤ 20 pct CR) determines that also for large thickness reductions the accumulated strain is highest in the core.

2. *Austenite stability in dependence of nitrogen content*

The stability of austenite against strain-induced martensite formation was evaluated from X-ray diffraction at various depths, as realized by electropolishing off thin layers (Figure 4). The surface zone remained entirely austenitic upon cold rolling; no indications for the presence of martensite (neither b.c.c. nor h.c.p.) were found at the surface. Evidently, a nitrogen content of 0.42 wt pct and associated change in microstructure/properties is (more than) sufficient to prevent detectable strain-induced martensite formation upon cold rolling for at least up to 70 pct thickness reduction.

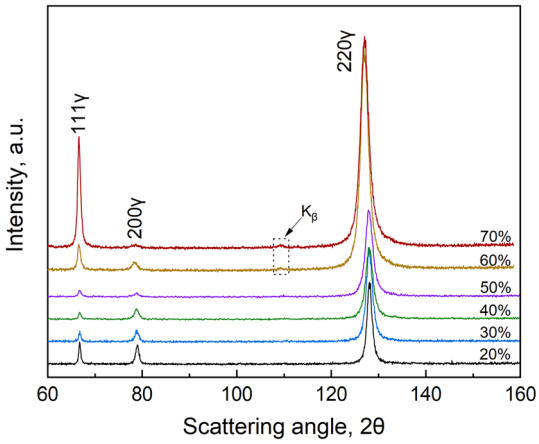

Fig. 4—X-ray diffractograms for the surface-adjacent zone of the solution-nitrided specimens after various degrees of cold rolling. An increase of the intensities of the 111 and 220 reflection is observed; peak broadening is evident for relatively high degrees of deformation.

In previous research,[29] X-ray diffraction analysis of annealed and solution-nitrided conditions demonstrated that the development of texture on plastic deformation results in a higher diffracted intensity of the 220_γ reflection in a symmetrical measurement set-up. A similar trend is observed here: initially, the intensities of 111_γ and 200_γ decrease, but 111_γ reappears for thickness reductions beyond 50 pct. No further investigation of the developing texture was performed, as this is beyond the scope of the present investigation. The presence of minor peaks indicated as K_β for the higher strain conditions (> 50 pct CR) originate from diffraction of CrK_β radiation by the {220} family of lattice planes. All peaks could be fitted excellently with a Voigt function with close to 100 pct Lorentzian broadening, indicating broadening caused by relatively small coherent domains. Broadening increases steadily with cold rolling reduction, implying a reduction in domain size. Line broadening is consistent with that observed in solution-nitrided and tensile deformed AISI 304 steel.[29]

Figure 5(a) shows representative X-ray diffractograms measured at different depths in the 60 pct cold-rolled specimen. The series of diffractograms reflects at which depth a particular combination of nitrogen content and cold work leads to strain-induced martensite formation. For the example given in Figure 5(a), the $211_{\alpha'}$ reflection appears at a depth of ~ 90 μm. The intensity of the $211_{\alpha'}$ reflection increases gradually with depth; other martensite peaks are observed beyond a depth of ~ 230 μm. Beyond a depth of ~ 430 μm, the obtained line profiles show only minor changes. The nitrogen–depth profile corresponding to 60 pct cold rolling in Figure 2(a) shows that the nitrogen content at ~ 430 μm has reached the core level. Relatively strong intensities of the 220_γ and the $211_{\alpha'}$ reflections typically exist in diffractograms for both the case and the core, consistent with the formation of the typical rolling texture in 304 steel, as measured in symmetrical set-up [35]. This indicates that the rolling texture developing on plastic deformation is dominant over the solution nitriding-induced texture in the surface zone (Figure 4). Not surprisingly, this applies particularly for heavily strained conditions, where the grains are severely elongated.

The depth where martensite becomes detectable, hereafter referred to as the *martensite start depth*, is given as a function of the cold rolling reduction in Figure 5(b). Cleary, this martensite start depth shifts towards the surface for larger thickness reductions. The nitrogen contents corresponding to these depths for the different strains reveal the thresholds of nitrogen content, beyond which the TRIP effect vanishes (Figure 5(c)).

An estimate of the volume fraction of α'-martensite was obtained from the χ-integrated intensities of all reflections for austenite and martensite (see Experimental). The volume fractions of α'-martensite in dependence of the degree of cold work and depth are collected in Figure 6(a). From the martensite start depth, the amount of martensite increases steadily and levels off on approaching the core, *i.e.*, beyond the nitrogen-containing case. The martensite content reached in the core increases with the degree of cold work, consistent with the

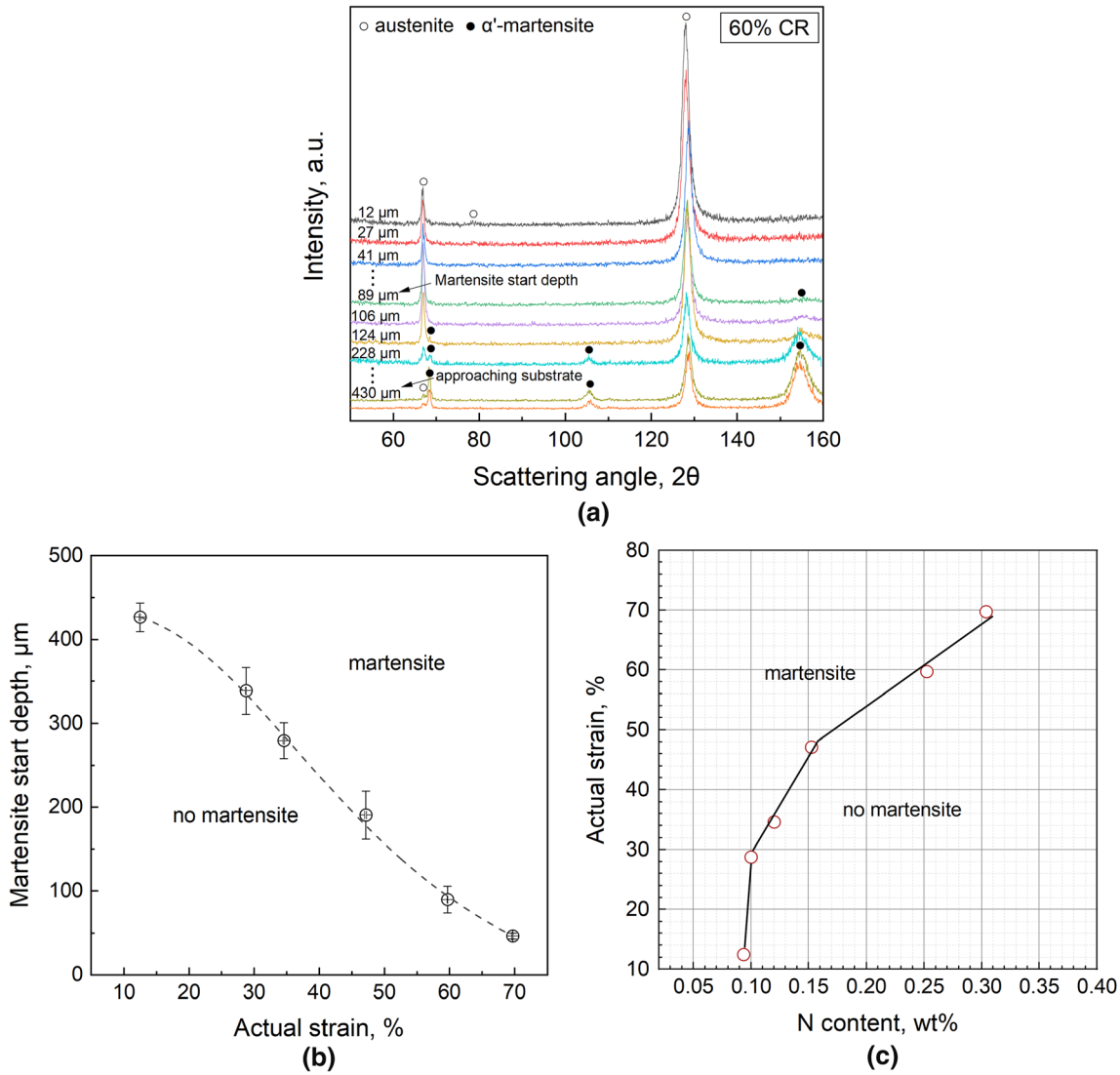

Fig. 5—(*a*) Representative X-ray diffractograms measured at different depths of a specimen after solution nitriding and 60 pct cold rolling; (*b*) martensite start depths for different rolling reductions; (*c*) threshold nitrogen content to avoid martensite formation during cold rolling of nitrogenated 304 steel.

previous results for austenitic stainless steels.[4,35–38] The dependence of martensite content with the local nitrogen content is given in Figure 6(b). For all investigated cold rolling conditions, the volume fraction of α'-martensite falls monotonically with increasing nitrogen content. For a particular nitrogen content, rolling reductions up to 60 pct lead to more deformation-induced martensite. Accordingly, for higher rolling reductions the threshold to avoid martensite formation is shifted to higher nitrogen contents. For 60 and 70 pct rolling reductions, the dependence of the martensite content on nitrogen content appears the same, apart from a higher martensite content in the core for 70 pct reduction.

3. *Characterization of the deformation microstructure*

a. Light optical microscopy Cross-sectional microstructures of the 304 steel after solution nitriding and additional cold rolling are provided in Figure 7. In all micrographs, the first ~ 700 μm below the surface is shown, so the deformed features in both nitrogen-enriched zone and core can be observed. After plastic deformation, the most significant change in microstructure is the elongation of grains along the rolling direction, which is more pronounced for higher strain. For a reduction above 40 pct, the initial coarse austenite grains (in the surface region) are no longer recognizable (Figures 7(d) through (f)). The fibrous structure formed in the sub-surface region of the specimen for 70 pct rolling reduction (Figure 7(f)) indicates that more homogeneous deformation is achieved at heavy strains, in agreement with the results in Figure 3.

In all deformed specimens, thin bands form throughout the specimen thickness. The density of such bands increases with increasing degree of cold rolling. Along with this, the morphology evolves from parallel bands to intersected bands. For moderately strained cases, *i.e.*, 20 to 40 pct thickness reduction, the microstructure in the

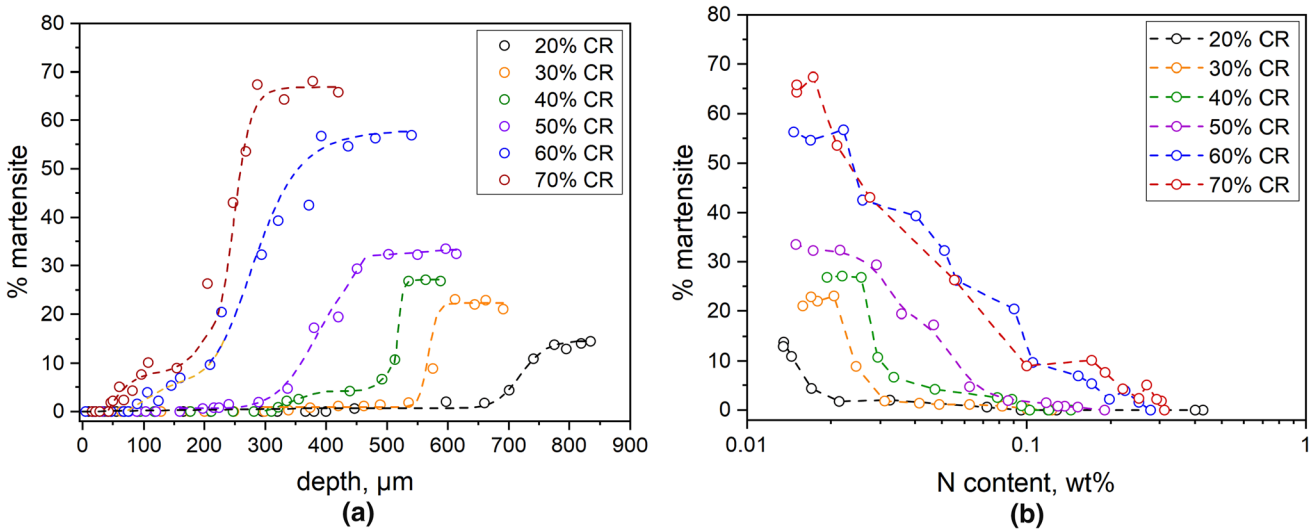

Fig. 6—The volume fraction of α′-martensite in nitrogen-alloyed 304 steel specimens as a function of (*a*) depth and (*b*) nitrogen content for various cold rolling reductions.

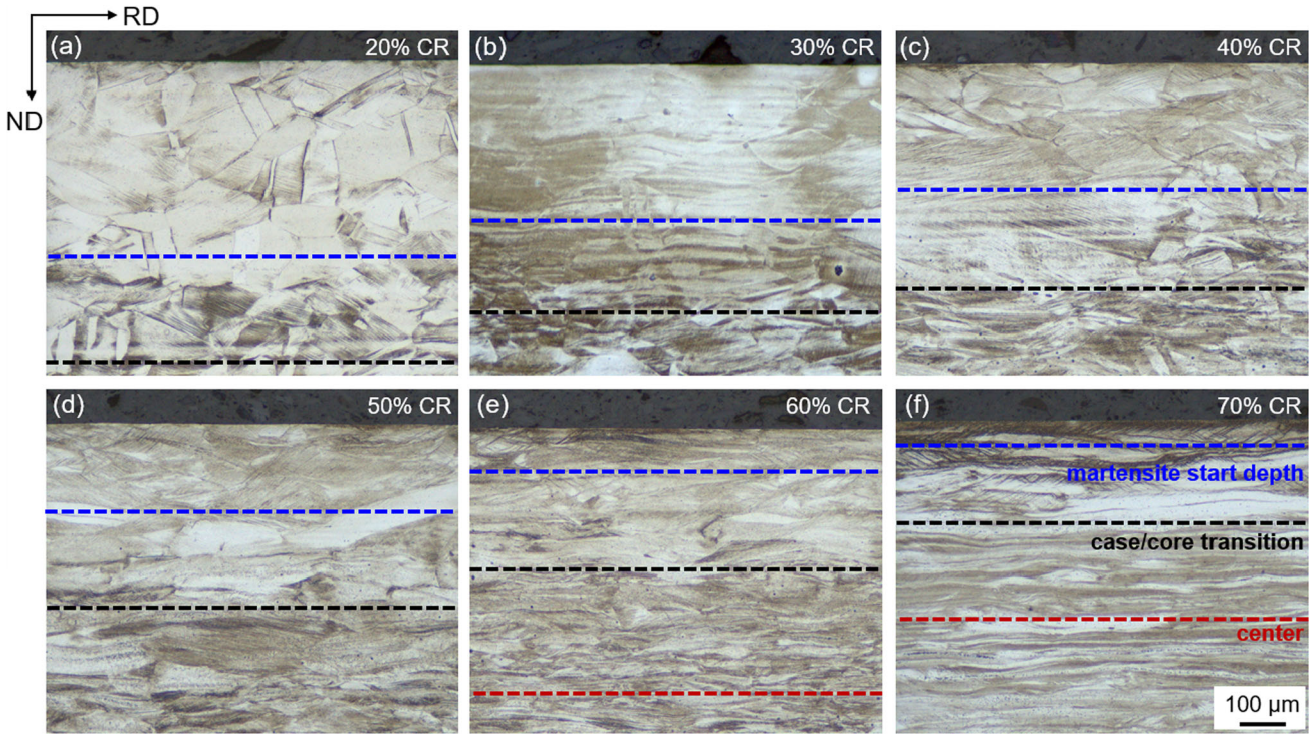

Fig. 7—Cross-sectional micrographs of 304 steel after solution nitriding and cold rolling 20 to 70 pct. The dotted horizontal lines in the micrographs mark the martensite start depth (blue), case/core transition (black) zone, and center (red) for each rolling reduction (Color figure online).

surface-adjacent zone remains relatively bright after etching, while the deformed sub-surface zone and the core appear dark. This is attributed to a better chemical resistance of the nitrogen-enriched austenite against the etchant and, in particular, to the absence of deformation-induced martensite. In heavily strained cases (≥ 50 pct thickness reduction), shear bands develop near the surface. The darkly etched shear bands in Figures 7(d) through (f) are inclined 40 to 45 deg with respect to RD. It was reported that for austenitic stainless steels shear banding leads to rhomb-shaped areas, which evolve into the lens-shaped domains for larger strain.[39] The present metallographic results are consistent with this. It is likely that the lens-shaped domains preferentially formed for relatively low nitrogen contents, where deformation leads to a mixture of twinned austenite and martensite.

4. *Scanning electron microscopy and electron backscatter diffraction*

A more detailed investigation of the deformation microstructure by means of ECCI and EBSD is given in Figure 8 for the 20 pct cold-rolled specimen. The ECC image in Figure 8(a) covers a cross section from the surface to a depth of ~ 1100 μm. The image shows the deformed microstructures in the nitrogen-enriched case and in the core. In the core region more thin bands have developed than in the nitrogen-enriched zone. In the latter, a few clean (band-free) and relatively large grains are found, in agreement with the metallographic observations in Figure 7(a). In the nitrogen-enriched zone, the ECC image shows more thin bands than the corresponding light optical image, because of the higher resolution obtained in ECCI. The four areas at different depths marked in Figure 8(a) were analyzed in more detail. In the core region, the thin bands developed discontinuously (Figure 8(b)) showing typical morphological features of mixed α' and ε-martensite, *i.e.,* lath α' units embedded in a single ε plate. The phase map in Figure 8(b1) confirms that the bands are composed predominantly of α'-martensite and a very small amount of ε-martensite. The orientation map indicates that six variants of α'-martensite are present in Figure 8(b2). This strongly suggests that plastic deformation has led to the formation of ε-martensite, which upon further straining has developed various variants of α'-martensite. It is expected that ε plates are overlaid by α'-martensite via stacking and coalescence of many small α'-martensite laths, optionally, of different orientation.[38] The $\gamma \rightarrow \varepsilon \rightarrow \alpha'$ transformation sequence in the un-nitrided core is in agreement with the previous research, which also stated that ε-martensite finally transforms into α'-martensite on augmenting the strain by repeated multiple rolling.[2,36,37] For 304L steel cold rolled from 10 to 90 pct thickness reduction, ε-martensite was only observed with X-ray diffraction for 10 pct reduction.[2] Even gentle manual polishing could induce the $\varepsilon \rightarrow \alpha'$ transformation, which might explain absence

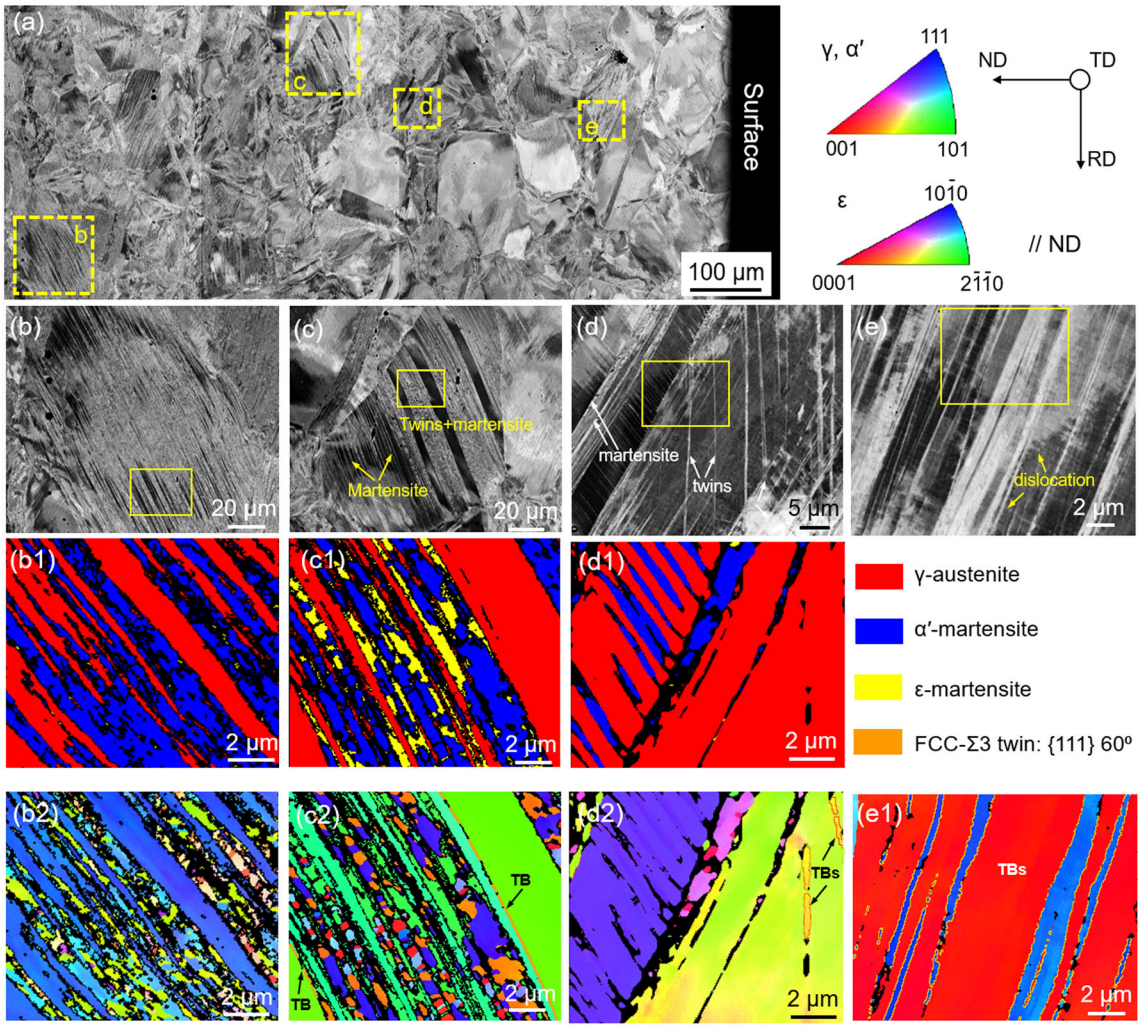

Fig. 8—Cross-sectional observations of 20 pct cold-rolled specimen showing the evolution of the microstructure in: (*a*) ECC image providing an overview. ECC images (*b*, *c*, *d*, and *e*) taken from the selected areas marked in (a). EBSD phase maps (b1, c1, and d1) and orientation maps (b2, c2, d2, and e1) parallel to ND, for the marked region in each of the ECC images. No phase transformation was identified in area (e), so no phase map is presented for this region.

of ε reflections in X-ray diffractograms (see References 12 and 13), where polishing was applied. This could also explain why the diffractograms obtained in the core region of the 60 pct cold-rolled specimen (Figure 5(a)) did not indicate the presence of ε-martensite.

The solution-nitrided case can be divided into two zones, a sub-surface zone and a surface zone, depending on whether or not deformation-induced martensite develops (Figure 5(b)). In the sub-surface zone, where the nitrogen content is relatively low, deformation-induced martensite as well as deformation-induced twins are observed (Figures 8(c) and (d)). The phase map in Figure 8(c1) further confirms the co-existence of α′- and ε-martensite, and particularly, the ECC image in Figure 8(c) shows that the initial deformation-induced ε plates lie parallel to the twin boundary (TB), *i.e.,* parallel to {111}. Furthermore, it is observed that those deformation twins, that do not intersect other twins or ε plates, do not support the nucleation of α′-martensite (Figures 8(c1) and 8(c2)). The growth of α′-martensite after the onset of ε-martensite formation and deformation twins is not constrained by adjacent parallel bands (ε or twins). This appears to be in contrast with the observations for intersections of ε plates and/or twins, or intersections of dislocation walls, which are considered insurmountable barriers for the growth of α′-martensite.[14,15] As the corresponding orientation map in Figure 8(c2) shows, some α′-martensite orientation variants are identified, while no obvious difference in orientation was detected in the components of ε-martensite that lie between the α′-martensite grains. The co-existence of twins, α′-martensite and ε-martensite, was also observed in carbon-alloyed 18Cr–8Ni–0.1C steel subjected to 15 pct cold rolling,[11] where the carbon addition would be responsible for a shift in deformation mechanism from strain-induced martensite to a combination of martensite formation and twinning.

Similarly, at ~ 440 μm depth (0.085 wt pct), the ECC image in Figures 8(d) through (d2) demonstrates the formation of twins and martensite, which moderately intersect. Apart from intermixed α′- and ε-martensite (as marked in d), the formation of blocky α′-martensite is identified (Figure 8(d1)). Blocky α′-martensite appears to have the same crystallographic orientation and thus represents a single variant (Figure 8(d) through (d2)). This observation suggests that the blocky α′-martensite evolved directly from γ, rather than from intermediate ε-martensite, which typically induces several variants of α′. Following the previous investigations,[40,41] these two types of martensite, *i.e.*, plates formed according to the $\gamma \rightarrow \varepsilon \rightarrow \alpha'$ path, and massive, $\gamma \rightarrow \alpha'$, are regarded as $(112)_\gamma$ and $(557)_\gamma$ types, respectively, where these martensites may present significantly different kinetics[42,43] and, hence, formation mechanisms.[40] A similar phenomenon was found in a 15 pct cold-rolled 18Cr–8Ni–0.1N steel, where α′-martensite was found to nucleate at the intersection of dislocation walls.[11] In the deformed sub-surface zone, joint TRIP and TWIP is enabled. Most likely, the dominant role of these deformation modes relates to the nitrogen content, such that more nitrogen promotes twinning. The observation for a depth of ~ 175 μm is shown in Figures 8(e) through (e1). In agreement with the XRD results, the relatively high nitrogen content in the surface zone indeed suppresses martensite formation during plastic deformation, and (bundles of) twins are clearly observed in this region (Figure 8(e1)). In addition, as another deformation product, the dislocation substructure is visible in areas with large twin spacing in the ECC image in Figure 8(e). A similar deformation structure was reported in Reference 44, wherein it was confirmed that the twin boundaries cut through the existing dislocation substructure that had developed during the early stages of deformation, without experiencing strong resistance. Evidently, in the high nitrogen surface zone, twinning and dislocation glide are the prevalent deformation mechanisms observed.

Figure 9 gives the deformation microstructure of the specimen after solution nitriding and 40 pct cold rolling. Following the ECCI observation in Figure 9(a), the deformation microstructure is characterized by elongated grains that contain more and finer bands than for the 20 pct strained specimen, and abundant band intersections. Three regions from the surface martensite-free zone, and two regions from the deformed sub-surface zone were selected for further analysis (marked in Figure 9(a)). The ECC image of region b (~ 40 μm below the surface) shows typical planar slip, which is generally observed in high nitrogen steels and has been proposed to be related to the short-range atomic ordering of nitrogen and chromium.[45] In this near-surface zone, where the nitrogen concentration is ~ 0.38 wt pct, dislocation slip is predominant and the formation of twins is hardly observed. At the other depths, 105 and 190 μm (corresponding N contents: ~ 0.3 and 0.2 wt pct), both slip and twinning are observed (Figures 9(c) and (d)), and the density of twins (bundles) appears to increase with depth, *i.e.*, decreasing nitrogen content. For a depth of 310 μm (~ 0.1 wt pct nitrogen), observations in Figures 9(e) through (e2) indicate the co-existence of twins, α′- and ε-martensite in the deformed microstructure, and nucleation of α′-martensite occurs essentially at intersections of bands. Similarly, deformed austenite microstructures were observed with TEM in 57 pct tensile-deformed 304 stainless steel.[4] In a deeper region (430 μm) where the nitrogen content is about 0.05 wt pct (Figures 9(f) through (f2)), twinning is not observed, while shear bands consisting of ε- and α′-martensite are present. Clearly, α′-martensite is the main deformation-induced product, as frequently observed within individual shear bands or in-between adjacent band sets.

C. *Hardness*

Hardness–depth profiles in 304 steels after solution nitriding and 20 to 70 pct cold rolling are given in Figure 10. For the unstrained HTSN case, the hardness reaches 275 $HV_{0.025}$ close to the surface and decreases gradually with depth until it reaches a constant value at ~ 575 μm, where the nitrogen content is about 0.075 wt pct (Figure 1(a)). Apparently, alloying with interstitial nitrogen below 0.075 wt pct, has no measurable

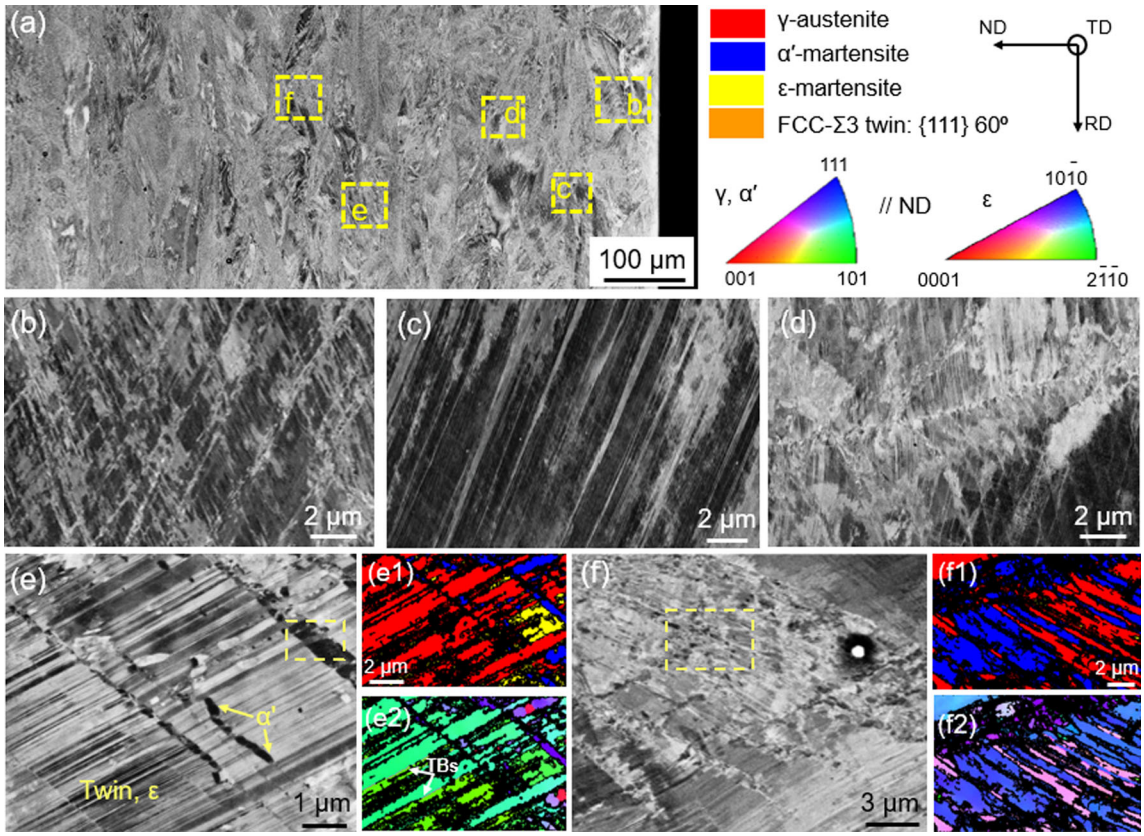

Fig. 9—Cross-sectional observations of 40 pct cold-rolled specimen showing the evolution of the microstructure in (*a*) ECC image providing an overview. ECC images of surface martensite-free zone (*b*, *c*, and *d*) and sub-surface zone (*e* and *f*) taken from the selected areas marked in (a). EBSD phase maps (e1 and f1) and orientation maps (e2 and f2) parallel to ND, for the marked region in each of the ECC images.

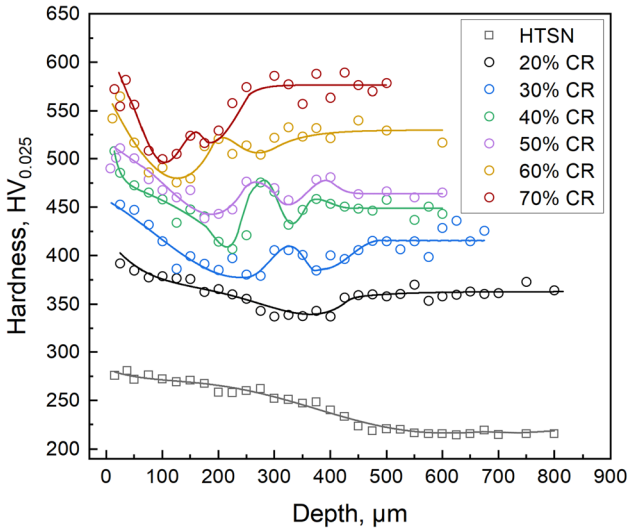

Fig. 10—Hardness–depth profiles of HTSN-treated 304 steel before and after plastic deformation.

effect on the bulk hardness (Figure 11(a)). Upon plastic straining, an increase in hardness is achieved in both the solution-nitrided zone and in the martensite-containing core. Surprisingly, there appears to be a softer region in-between case and core. The observed "softer" intermediate depth range is more pronounced for higher strains, as is particularly apparent for the 70 pct reduction. Obviously, the hardness increase in the core of the specimen is associated with strain-induced martensite formation, which can only occur below a threshold nitrogen content of ~ 0.3 wt pct N for large reductions (see Figure 6(b)).

IV. DISCUSSION

A. *Effect of Interstitial Nitrogen on Deformation Microstructure*

The combined results of ECCI and EBSD analysis allow to assign the deformation mechanism in dependence of nitrogen content and plastic strain, as shown in Table I. Upon plastic straining the solution-nitrided 304 steel accommodates the plastic deformation throughout the plate thickness by dislocation glide, twinning and deformation-induced martensite formation. The associated deformation response, *e.g.*, TRIP and/or TWIP, depends on the combination of nitrogen content and (actual) strain. As confirmed by both XRD and EBSD analysis, a nitrogen concentration threshold exists to achieve/guarantee TWIP effects for a certain plastic strain (Figures 5(c), 8 and 9). It should be noted that for relatively high strains (> 50 pct CR) the nitrogen content necessary to prevent martensite formation increases strongly with the strain.

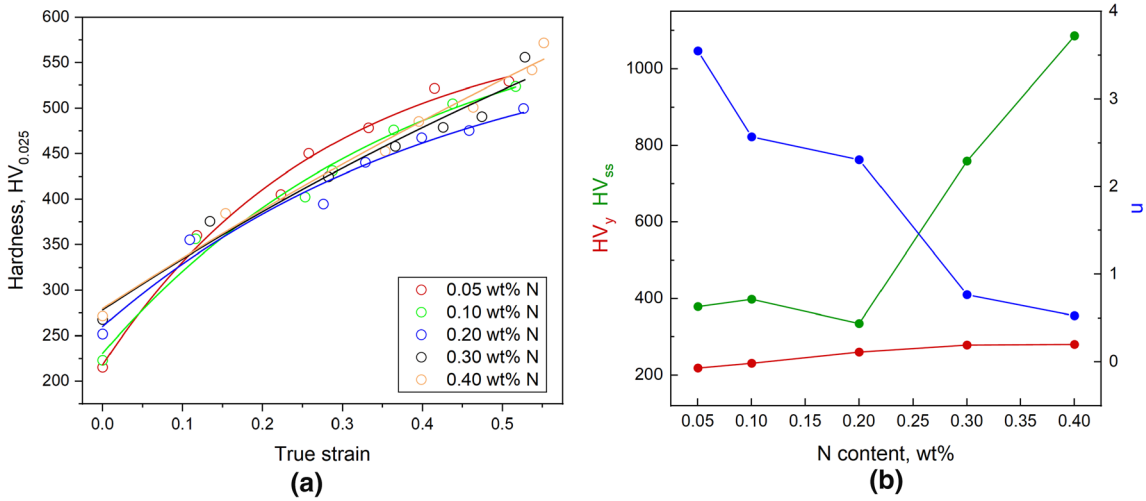

Fig. 11—(*a*) Hardness increase as a function of the true strain for the selected nitrogen concentrations (data points) and fitted Voce equation (lines). (*b*) Values obtained with fitting of the Voce equation.

For all strain levels in the relatively high nitrogen content range, *i.e.*, beyond the threshold, deformation-induced martensite formation was avoided. As previously stated for high nitrogen steels,[46] at lower strains ($\varepsilon < 5$ pct) concerted planar glide of leading and trailing partial dislocations governs the evolution of the microstructure, irrespective of nitrogen content. At higher strains, dislocation glide and twinning establish deformation. The critical conditions for the onset of twinning during cold deformation depend on the nitrogen content, and generally, shift towards lower strains with increasing the nitrogen content.[41] Consistent with these literature observations, in the present case, the deformation microstructure in the high nitrogen surface-adjacent zone reveals glide and twinning (20-1, 40-1 through 40-3 in Table I). It is anticipated that the density of twins varies and that dislocation glide applies for the entire range of investigated nitrogen contents. Considering the orientation-dependent twinning behavior and the variation in nitrogen content that exists within relatively coarse grains, a specimen subjected to relatively low strain would not be suitable to estimate the variation in the contribution of twinning to the total deformation. The contribution of twinning can be assessed with metallographic examination for moderate strain conditions or from EBSD and ECCI investigation of relatively heavy strain cases. Comparison of the deformation microstructures for cases 40-1 to 40-3 indicates that, for a certain strain level (*i.e.*, $\varepsilon = 42 \pm 2$ pct), the contribution of twinning decreases with increasing nitrogen content and is negligible close to the surface, where the nitrogen content exceeds 0.38 wt pct. For a nitrogen content of ~ 0.3 wt pct (20-1 and 40-2 in Table I), coordination between slip and twinning is observed in both 20 and 40 pct rolling conditions. The twinned microstructure initiates at an early stage of rolling and remains at a high strain levels.

For the depths where the nitrogen content is below the threshold necessary to stabilize austenite, deformation-induced martensite developed and both transformation sequences $\gamma \rightarrow \varepsilon \rightarrow \alpha'$ and $\gamma \rightarrow \alpha'$ were identified. At the same strain level of ~ 33 pct, a higher nitrogen content leads to additional deformation by twinning, without altering the martensite formation sequence (ref. 20-4 and 40-4 in Table I). Despite the co-existence of martensite formation and twinning in both 20-2 and 40-4 cases, different martensitic transformation mechanisms were noted, associated with the significant differences in strain condition (12 vs. ~ 33 pct) and a minor difference in nitrogen content (0.085 vs. 0.1 wt pct). As mentioned above, $\varepsilon \rightarrow \alpha'$ transformation would continuously proceed, because of the repeated multiple rolling, suggesting less intermediate ε-martensite for large strains. It then follows that the observed α'-martensite at a gentle strain (*i.e.,* 12 pct) is directly formed from austenite, associated with the local nitrogen content rather than the applied strain (20-2, 20-3 and 40-4). It potentially shows that the martensitic transformation mechanism is affected by the nitrogen content, especially in a relatively low nitrogen content range, *e.g.,* 0.05 to 0.1 wt pct. Moreover, for a nitrogen content of 0.05 wt pct, twins that developed at a strain of 12 pct had disappeared when the rolling reduction is increased to 53 pct (20-3 and 40-5 in Table I), suggesting that de-twinning occurred. Similar phenomena were also observed at a later stage of uniaxial tensile deformation (high strain range) in a 304 stainless steel.[4]

B. *Effect of Deformation Mechanism on Hardness*

The hardness–depth profiles as presented in Figure 10 show an initial decline with nitrogen content, followed by a hardness minimum and fluctuations, before reaching a stable level in the core. The hardness reached is the net result of the contributions of several strengthening mechanisms: solid solution strengthening, work hardening by dislocation–dislocation interaction, and TWIP/TRIP. For different depth ranges, these mechanisms apply in various combinations.

Table I. Deformation Response to Different Combinations of Nitrogen Content and Actual Strain, Collected at Various Depths in 20 and 40 Pct Deformed 304 Steels

Reduction		Depths, μm	N Content, Pct	Strain, Pct	Predominant Deformation Structure
20 Pct CR	20-1	175	0.27	10	twins and dislocation
	20-2	440	0.085	12	α'-martensite and twins
	20-3	550	0.05	12	α'- and ε-martensite, twins
	20-4	960	0.024	~ 33	α'- and ε-martensite
40 Pct CR	40-1	40	0.38	44	dislocation
	40-2	105	0.3	42	dislocation and twins
	40-3	190	0.2	40	twins and dislocation
	40-4	310	0.1	33	α'- and ε-martensite, twins
	40-5	430	0.05	53	α'- and ε-martensite

Figure 11(a) summarizes the evolution of hardness with the true strain, as calculated from the thickness reduction (pct cold work), for five different nitrogen contents. Recognizing the interdependence of hardness and yield strength, the Voce equation was adopted to fit the data:

$$HV(\varepsilon) = HV_y + HV_{ss}\{1 - e^{-n\varepsilon}\}, \qquad []$$

where ε is the true strain, HV_y and HV_{ss} are the hardness values in proportion to the yield strength and at the saturation stress (*i.e.*, infinite plastic deformation), respectively; n is the work hardening exponent. Good convergence was obtained on fitting the data with the Voce equation. The values of the fitting parameters HV_y, HV_{ss}, and n are given in Figure 11(b) as a function of the nitrogen content. HV_y and HV_{ss} increase with nitrogen content, while the work hardening exponent n decreases. The change in n reflects the change in governing deformation mechanism from TRIP at low N content to slip at high N contents. The contribution of solid solution strengthening by nitrogen is reflected by the increase in HV_y in Figure 11(b). The role of nitrogen becomes particularly clear from considering the hardness value corresponding to the saturation strength HV_{ss} in Figure 11(b). Obviously, work hardening by dislocation–dislocation interaction becomes more effective by dissolving nitrogen. A reduction in nitrogen content from 0.4 to 0.2 wt pct shows a decrease in the hardness values corresponding to yield strength and strain saturation (Figure 11(b)), while the work hardening exponent increases. This is in agreement with earlier work, that showed that dissolving more nitrogen led to a decrease in the work hardening exponent, as derived from tensile testing and evaluated by the Voce equation.[29]

The hardness minimum and the fluctuations in the hardness profiles occur in the composition range where the nitrogen content is insufficiently high to affect work hardening by dislocation–dislocation interaction, but sufficiently high to keep the content of martensite relatively low. This is demonstrated in Figure 12 for selected martensite contents and hardness distributions, as earlier presented in Figures 6(a) and 10. For the 60 and 70 pct cold-rolled conditions, the minimum in the hardness distribution is reached for martensite contents

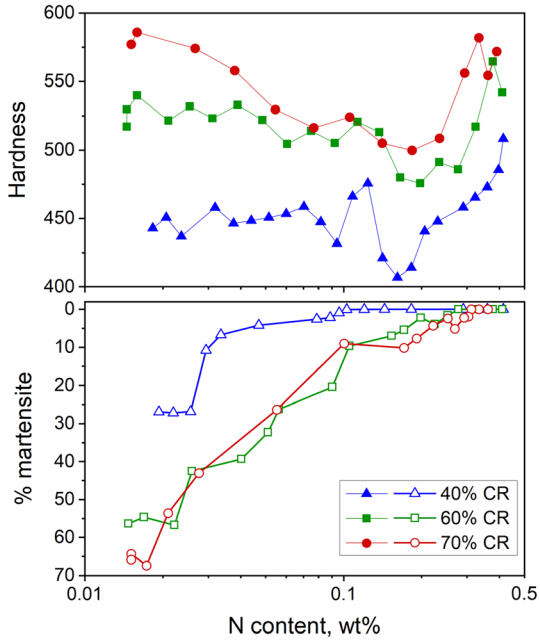

Fig. 12—Hardness and martensite content distributions reproduced from Figs. 6(a) and 10(a). Filled markers refer to hardness, open markers refer to martensite content.

below 10 pct. An increase in hardness for the 60 and 70 pct cold-rolled specimens coincides with a steep increase in martensite content above 10 pct. For the 40 pct cold-rolled specimen, martensite is first detected beyond a nitrogen content of 0.12 wt pct. For slightly higher nitrogen contents, a local maximum in hardness is observed, which coincides with the presence of a high density of twins (cf. Figure 9(e)). Therefore, it is suggested that the hardness fluctuations in Figure 10(a) reflect the combinations of prevalent deformation mechanisms. A high density of deformation twins can contribute to local hardness maxima.

C. *Influence of Nitrogen Content on Stacking Fault Energy*

The evolution of different deformation mechanisms during cold deformation is generally explained in terms of the stacking fault energy. A very low stacking fault

energy would promote strain-induced martensite formation, while a high stacking fault energy promotes dislocation glide. Deformation twinning would apply for intermediate values of the SFE. Within the constraints of this paradigm, the present observations indicate that adding nitrogen is an effective means of adjusting the SFE and tailoring the (combination of) deformation mechanism(s) in stainless steels, consistent with earlier work on homogenously solution-nitrided stainless steels.[29] Following the reviews given by Schramm[9] and Das,[26] SFE values of austenitic stainless steels range from ~ 10 to 100 mJ m^{-2}. For Fe–Cr–Ni alloys containing nitrogen contents in the range investigated in the present work, *i.e.*, from 0.024 to 0.44 wt pct N, mutually exclusive points of view have been published. Nitrogen could either augment[39,45,47,48] or reduce[9,46] the SFE. This discrepancy originates from several aspects, involving experimental methodology to determine SFE, the composition of the base material, range of nitrogen content, grain size, *etc*. Adding nitrogen could cause opposite changes in the SFE of alloys, depending on the host composition[23,46] and the results from a limited range of nitrogen contents would not be sufficient to draw unequivocal conclusions on the effect on the SFE.[24] The present approach for a continuous range of nitrogen contents for the same alloy, in combination with applied deformation, clearly demonstrates that the continuous change in deformation mechanism from high to low N content, is consistent with a continuous decrease in SFE. For the 11 ± 1 pct rolling reduction condition (Table I), the dominant deformation modes change from TRIP/TWIP to TWIP/slip. In the current paradigm of the relation between SFE and deformation mechanisms, this indicates an increase in the value of SFE for nitrogen content in the range 0.05 to 0.27 wt pct. Similarly, referring to the evolution from TWIP/slip to slip, an increase in SFE values is evidenced for N in the range 0.2 to 0.38 wt pct at a strain level of 42 ± 2 pct. For an actual strain of ~ 33 pct, additional twinning developed at 0.1 wt pct N, which again indicates an increase in SFE with N content. Evidently, the present set of data consistently indicates that the value of SFE of 304 stainless steel gradually increases with an increment in the nitrogen content, where the investigation refers to the nitrogen content range of 0.024 to 0.38 wt pct.

Further, it is noted that for all experimental approaches to assess the SFE, the assumption is that the SFE is always positive. Recently, the validity of this assumption has been questioned for metastable alloys,[49] which rather should be assigned a negative SFE, in accordance with their thermodynamic metastability as reflected by and M_s (and thus T_0) above room temperature. Hence, austenite in the present case experiences a driving force to transform. In this context, the experiments show that nitrogen changes the SFE for AISI 304 from a negative value, for which martensite forms, to a positive value, where austenite is stable. Computational approaches to elucidate the influence of nitrogen on SFE for various alloy compositions may shed a light on this, but no consensus has so far been reached.[50,51] A remedy to determine negative SFEs experimentally was proposed,[22] but requires a series of experiments for the same material with different grain sizes.

V. CONCLUSION

A graded component with a depth gradient in nitrogen content was manufactured from 304 stainless steel plate using high-temperature solution nitriding. Plastic deformation of the graded material by cold rolling provides access for characterization of the phase stability and dominant deformation modes for a continuous range of nitrogen contents at various plastic strains. The primary findings are as follows:

- For all applied strain conditions, an increase in nitrogen content contributes to the phase stability of austenite against plastic deformation.
- For the nitrogen content range 0.024 to 0.30 wt pct, the threshold nitrogen content required to prevent strain-induced martensite formation increases with straining. In particular, a remarkable increase in threshold nitrogen content occurs for engineering strain levels beyond 50 pct.
- The predominant deformation modes depend strongly on the nitrogen content. For a particular strain, in order of increasing nitrogen content, the deformation mode essentially featured (i) strain-induced martensite formation, (ii) co-existence of martensite formation and twinning, and (iii) twinning and dislocation glide.

This study illustrates the advantage of the presented experimental approach that is necessary to understand the relationship between nitrogen content, strain, and deformation mechanism. The findings contribute to future design of nitrogen-containing austenitic stainless steels to tailoring microstructures and associated mechanical properties.

ACKNOWLEDGMENTS

The Independent Research Fund Denmark under Grant Number 9041-00145B is gratefully acknowledged. The research leading to these results has received funding from the European Union's Horizon 2020 research and innovation programme under the Marie Sklodowska-Curie Grant Agreement No. 713683 (COFUNDfellowsDTU) and No. 841108 (MSCA-IF).

CONFLICT OF INTEREST

On behalf of all authors, the corresponding author states that there is no conflict of interest.

REFERENCES

1. K.H. Lo, C.H. Shek, and J.K.L. Lai: *Mater. Sci. Eng. R Rep.*, 2009, vol. 65, pp. 39–104.
2. A. Hedayati, A. Najafizadeh, A. Kermanpur, and F. Forouzan: *J. Mater. Process. Technol.*, 2010, vol. 210, pp. 1017–22.
3. A. Das, P.C. Chakraborti, S. Tarafder, and H.K.D.H. Bhadeshia: *Mater. Sci. Technol.*, 2011, vol. 27, pp. 366–70.
4. Y.F. Shen, X.X. Li, X. Sun, Y.D. Wang, and L. Zuo: *Mater. Sci. Eng. A*, 2012, vol. 552, pp. 514–22.
5. Y.F. Shen, Y.D. Wang, X.P. Liu, X. Sun, R. Lin Peng, S.Y. Zhang, L. Zuo, and P.K. Liaw: *Acta Mater.*, 2013, vol. 61, pp. 6093–6106.
6. T. Tsuchiyama, H. Takebe, K. Tsuboi, and S. Takaki: *Scr. Mater.*, 2010, vol. 62, pp. 731–34.
7. T. Tsuchiyama, K. Tsuboi, S. Iwanaga, T. Masumura, A. Macadre, N. Nakada, and S. Takaki: *Scr. Mater.*, 2014, vol. 90, pp. 14–16.
8. N. Solomon and I. Solomon: *Eng. Fail. Anal.*, 2017, vol. 79, pp. 865–75.
9. R.E. Schramm and R.P. Reed: *Metall. Trans. A*, 1975, vol. 6, pp. 1345–51.
10. Y. Tian, O.I. Gorbatov, A. Borgenstam, A.V. Ruban, and P. Hedström: *Metall. Mater. Trans. A Phys. Metall. Mater. Sci.*, 2017, vol. 48, pp. 1–7.
11. T. Masumura, N. Nakada, T. Tsuchiyama, S. Takaki, T. Koyano, and K. Adachi: *Acta Mater.*, 2015, vol. 84, pp. 330–38.
12. B. Wang, C. Hong, G. Winther, T.L. Christiansen, and M.A.J. Somers: *Materialia*, 2020, vol. 12, p. 100751.
13. M.A.J. Somers: in *Proceedings of the 26th IFHTSE Congress*, Moscow, 2019, pp. 22–29.
14. O. Grässel, L. Krüger, G. Frommeyer, and L.W. Meyer: *Int. J. Plast.*, 2000, vol. 16, pp. 1391–1409.
15. J.W. Simmons: *Mater. Sci. Eng. A*, 1996, vol. 207, pp. 159–69.
16. M.O. Speidel: *Materwiss. Werksttech.*, 2006, vol. 37, pp. 875–80.
17. M.O. Speidel: *Inst. Met. London*, 1989, p. 92.
18. T.H. Lee, C.S. Oh, and S.J. Kim: *Scr. Mater.*, 2008, vol. 58, pp. 110–13.
19. A. Kundu, D.P. Field, and P. Chandra Chakraborti: *Mater. Sci. Eng. A*, 2020, vol. 773, p. 138854.
20. S. Allain, J.P. Chateau, O. Bouaziz, S. Migot, and N. Guelton: *Mater. Sci. Eng. A*, 2004, vol. 387–389, pp. 158–62.
21. T.H. Lee, E. Shin, C.S. Oh, H.Y. Ha, and S.J. Kim: *Acta Mater.*, 2010, vol. 58, pp. 3173–86.
22. K.V. Werner, F. Niessen, M. Villa, and M.A.J. Somers: *Appl. Phys. Lett.*, 2021, vol. 119, pp. 141902-1-41902–6.
23. L. Vitos, J.O. Nilsson, and B. Johansson: *Acta Mater.*, 2006, vol. 54, pp. 3821–26.
24. J. Talonen and H. Hänninen: *Acta Mater.*, 2007, vol. 55, pp. 6108–18.
25. J. Lu, L. Hultman, E. Holmström, K.H. Antonsson, M. Grehk, W. Li, L. Vitos, and A. Golpayegani: *Acta Mater.*, 2016, vol. 111, pp. 39–46.
26. A. Das: *Metall. Mater. Trans. A Phys. Metall. Mater. Sci.*, 2016, vol. 47, pp. 748–68.
27. H. Berns: *ISIJ Int.*, 1996, vol. 36, pp. 909–14.
28. H. Berns and S. Siebert: 1996, vol. 36, pp. 927–31.
29. F. Bottoli, G. Winther, T.L. Christiansen, K.V. Dahl, and M.A.J. Somers: *Metall. Mater. Trans. A Phys. Metall. Mater. Sci.*, 2016, vol. 47, pp. 4146–59.
30. R.D. Arnell: *J. Iron Steel Inst.*, 1968, pp. 1035–36.
31. R.W. Hinton: *J. Test. Eval.*, 1987, vol. 15, pp. 95–100.
32. H. Pawelski: *J. Mater. Process. Technol.*, 2002, vol. 125–126, pp. 392–97.
33. W. Lehnert and R. Kawalla: *Steel Res. Int.*, 2005, vol. 76, pp. 142–47.
34. X.F. Fang and W. Dahl: *Mater. Sci. Eng. A*, 1991, vol. 141, pp. 189–98.
35. B. Ravi Kumar, A.K. Singh, S. Das, and D.K. Bhattacharya: *Mater. Sci. Eng. A*, 2004, vol. 364, pp. 132–39.
36. M. Hadji and R. Badji: *J. Mater. Eng. Perform.*, 2002, vol. 11, pp. 145–51.
37. V. Shrinivas, S.K. Varma, and L.E. Murr: *Metall. Mater. Trans. A*, 1995, vol. 26A, pp. 661–71.
38. L.E. Murr, K.P. Staudhammer, and S.S. Hecker: *Metall. Trans. A*, 1982, vol. 13, pp. 627–35.
39. C. Donadille, R. Valle, P. Dervin, and R. Penelle: *Acta Metall.*, 1989, vol. 37, pp. 1547–71.
40. H. Schumann: *Pract. Metallogr.*, 1989, vol. 26, pp. 335–52.
41. P.G. McDougall and C.M. Wayman: *ASM Int. Martensite, 1992,* 1992, pp. 59–95.
42. M. Villa and M.A.J. Somers: *Scr. Mater.*, 2018, vol. 142, pp. 46–49.
43. M. Villa and M.A.J. Somers: *HTM J. Heat Treat. Mater.*, 2020, vol. 75, pp. 263–86.
44. I. Gutierrez-Urrutia and D. Raabe: *Acta Mater.*, 2011, vol. 59, pp. 6449–62.
45. V.G. Gavriljuk, H. Berns, C. Escher, N.I. Glavatskaya, A. Sozinov, and Y.N. Petrov: *Mater. Sci. Forum*, 1999, vol. 318, pp. 455–60.
46. P. Müllner, C. Solenthaler, P. Uggowitzer, and M.O. Speidel: *Mater. Sci. Eng. A*, 1993, vol. 164, pp. 164–69.
47. V. Gavriljuk, Y. Petrov, and B. Shanina: *Scr. Mater.*, 2006, vol. 55, pp. 537–40.
48. M. Ojima, Y. Adachi, Y. Tomota, Y. Katada, Y. Kaneko, K. Kuroda, and H. Saka: *Steel Res. Int.*, 2009, vol. 80, pp. 477–81.
49. X. Sun, S. Lu, R. Xie, X. An, W. Li, T. Zhang, C. Liang, X. Ding, Y. Wang, H. Zhang, and L. Vitos: *Mater. Des.*, 2021, vol. 199, p. 109396.
50. I.A. Yakubtsov, A. Ariapour, and D.D. Perovic: *Acta Mater.*, 1999, vol. 47, pp. 1271–79.
51. S. Kibey, J.B. Liu, M.J. Curtis, D.D. Johnson, and H. Sehitoglu: *Acta Mater.*, 2006, vol. 54, pp. 2991–3001.